# Photo- and Photo-Fenton-like Catalytic Degradations of Malachite Green in a Water Using Magnetically Separable ZnFe$_2$O$_4$-reduced Graphene Oxide Hybrid Nanostructures

**H. Y. He[1*], J. F. Huang[1] and J. Lu[1]**

[1]*College of Material Science and Engineering, Shaanxi University of Science and Technology, Xi'an, Shaanxi, 710021, China.*

***Authors' contributions***

*This work was carried out in collaboration between all authors. All authors read and approved the final manuscript.*

*Original Research Article*

---

## ABSTRACT

ZnFe$_2$O$_4$ nanoparticles and ZnFe$_2$O$_4$-reduced graphene oxide (ZnFe$_2$O$_4$-rGO) hybrid nanostructures with rGO/ZnFe$_2$O$_4$ ratio of 0.05, and 0.10 were hydrothermally synthesized. The microstrutrual and photocatalytic activities of nanoparticles and hybrids were studied in the photodegradation of malachite green in the water. The ZnFe$_2$O$_4$ nanoparticles and theirhybrids showed uniform granular morphology and average particle sizes below ~16 nm. Because higher valence band energy of the ZnFe$_2$O$_4$, the photogenerated electrons can be transformed from the ZnFe$_2$O$_4$ to the rGO. Therefore, the sunlight-excited photocatalytic and Fenton-like photocatalytic activities of hybrids in the dye degradation showed obviously greater than the nanoparticles and increased with increasing rGO/ZnFe$_2$O$_4$ ratio. Moreover, the photodegradation rate is larger at higher initial solution pH=5 than at pH=7, whereas the photo-Fenton-like reaction is intenser at higher H$_2$O$_2$ concentration. The quasi-kinetic rate constants of the photocatalysis systems are in

---

*Corresponding author: E-mail: hehy@sust.edu.cn;*

the range of ~0.412–0.96 $h^{-1}$ and increase to ~3.86–7.53 $h^{-1}$ by synthetically using $H_2O_2$. The nanoparticles and hybrids also showed strong ferromagnetic property with the saturation magnetization of ~25.15–26.28 emu/g, which provides a well magnetic separation performance of the nanoparticles and hybrids from the degraded solution.

*Keywords: Graphene; hybrids; heterojuction; photocatalysis; Fenton-like reaction; magnetic separation.*

## 1. INTRODUCTION

The graphene possesses the ability to accept the electrons from semiconductor, so can prevent recombination of photogenerated electrons and holes. Anchoring well-structured photocatalysts onto graphene-based materials can explore novel composites with advanced photocatalytic performances. Therefore, the introduction of graphene-related materials (graphene, graphene oxide, and reduced graphene oxide) as catalyst supports into the various photocatalytic systems has attracted great interest [1-3]. The hybrid products were found to display outstanding photocatalytic performances [4–15].

Zinc ferrite is magnetic semiconductor with narrow optical bandgap, innocuity and low cost. The strong magnetic property of this material can provide a well magnetic separation performance from the aqueous solution as used as a photocatalyst. Thus, the $ZnFe_2O_4$ should be reasonable for structuring the semiconductor-rGO hetero- junctions with excellent photocatalytic activity.

In the current work, we focus on (i) the hydrothermal synthesis and microstructures of $ZnFe_2O_4$ nanoparticles and $ZnFe_2O_4$-rGO hybrids; (ii) Investigation of the effects of the rGO/$ZnFe_2O_4$ ratio on the photocatalytic and Fenton-like photocatalytic activities of the synthesized hybrids in photodegradation of malachite green dye in the water.

## 2. EXPERIMENTAL

### 2.1 Materials

The starting materials used were all analytic grade chemicals without any further processing. Graphene oxide (GO, Jining LeaderNano Tech L.L.C., China). Zinc nitrate ($Zn(NO_3)_2 \cdot 6H_2O$, Shenyang Hua Bai Tai Chemical Co. Ltd, China) and iron nitrate ($Fe(NO_3)_3 \cdot 9H_2O$, Beijing Baishunchem. Co. Ltd., China) were used as starting materials. Sodium hydroxide (NaOH, Tianjing Zhiyuan chemical agent. Co. Ltd., China)

was used to synthesize the photocatalysts. The malachite green ($C_{23}H_{25}ClN_2$, Tianjing Basifu chemical L.L.C., China) and hydrogen peroxide aqueous solution ($H_2O_2$, ≥30%, Tianjing Beicheng chemical agent. Co. Ltd., China)) were used in the photocatalysis experiments.

### 2.2 Methods

For the synthesis of $ZnFe_2O_4$ nanoparticles, the chemicals were dissolved in 15 ml deionized water according to the required stoichiometric proportions of $ZnFe_2O_4$. The concentration of $Fe^{3+}$ in the such solutions was all 0.2 mol $l^{-1}$. NaOH with triple gram equivalents of all metal cations was dissolved in small amount of deionized water (~3 ml) and completely dropped into the solutions with magnetic stirring. This relative large amount of NaOH addition can assures the solution pH>10 throughout and so full precipitation of the all cations. The precursor solutions were then transferred into autoclaves (volume: 25 ml, degree of filling: ~80 vol.%). After sealing, the hydrothermal reaction was then carried out in a oven at 180°C for 24 h. After natural cooling in the oven, the products were washed repeatedly with distilled water until washing water pH~7, and then dried at 100°C for 24 h. With same method, the $ZnFe_2O_4$-rGO hybrids were synthesized by directly dissolving the zinc nitrate and iron nitrate into the GO aqueous solution according to the mass ratio of GO/$ZnFe_2O_4$ of 0.05 and 0.10. The GO aqueous solution was prepared by ultrasonically dispersing GO in deionized water.

### 2.3 Characterization

The crystalline structural phase of the synthesized nanoparticles and hybrids was identified at room temperature using an X-Ray diffractometer (XRD, $CuK_{\alpha1}$, λ=0.15406 nm, Model No: D/Max--2200PC, Rigaku, Japan). The morphology of the nanoparticles and hybrids was analyzed using field emission scanning electron microscope (SEM, Model No: S-4800, Hitachi, Japan). Raman spectra of the samples were collected using a spectrophotometer (Model no:

Renishaw-invia, U.K.) at a laser excitation wavelength of 532 nm. Fourier transform Infrared spectrum (FTIR) spectra were determined by infrared spectroscopy (Model no: Vector-22, Bruker, Germany).The hybrids were adhered on the glass slides with thin transparent adhesive agent, in order that the transmittance, reflectance and absorbance spectra of the nanoparticles and hybrids were determined with an ultraviolet-visible spectrophotometer (Model No: UV2600, SDPTOP, Shanghai, China). The magnetic property was measured with a vibrating sample magnetometer (VSM, Model No: Versa Lab, Quantun Design, USA). The range of applied field is from -30 kOe to 30 kOe. Magnetic separation performance of the samples was evaluated by attracting the photocatalyst from the degraded solution with a permanent magnet.

To investigate the photocatalytic activity of the synthesized photocatalysts. The malachite green ($C_{23}H_{25}ClN_2$, Tianjing Basifu chemical L.L.C., China) is used as a substrate and dissolved in deionized water to form aqueous solution with a concentration of $5 \times 10^{-6}$ M. One group of the solution were additionally adjusted to initial pH=5 with diluted HCl aqueous solution. In each experiment, 50 ml malachite green aqueous solution and 50 mg synthesized photocatalysts were added into a glass beaker. In two other groups of the solutions with pH=7, 0.5 ml and 1.0 ml hydrogen peroxide aqueous solution (30%) were added, respectively. The photocatalysis experiment was carried out under the sunlight with average intensities of ~400 W/m$^2$. After different irradiation times, ~3 ml solutions were taken out and measured for their absorbances on a spectrophotometer (Model No: 722N, Hengping, China). The solutions after the test were returned to the breakers to maintain the normal volume of the solutions under test.

In first hour of the above process, the oxidation-reduction potentials (ORP) of the malachite green aqueous solutions in all photocatalytic conditions were measured with an oxidation-reduction potential tester (Model no: ORP-286, China). The ORP of the nanoparticles and hybrids surfaces were evaluated by the differences of the oxidation-reduction potentials of the malachite green aqueous solutions with and without the photocatalysts.

The quasi-kinetic rate constant ($k_1$) was calculated with the kinetic relation between the concentration ($C$) of the malachite green in the water and the photocatalytic reaction time ($t$) given by:

$$\frac{C}{C_0} = e^{-k_1 t} \qquad (1)$$

In which, $C_0$ is the initial concentration.

# 3. RESULTS AND DISCUSSION

## 3.1 XRD Analysis

Fig. 1a shows the XRD patterns of the synthesized nanoparticles and hybrids. All diffraction peaks match with the reported powder diffraction data of hexogonal $ZnFe_2O_4$ (JCPDS: 79-1150). Crystallites size (D) was estimated from the full width (in radian) at half maximum ($\beta$) of the diffraction peak at $2\theta \sim 35.5°$ according to the Scherrer's equation:

$$D = 0.9 \frac{\lambda}{\beta \cos\theta} \qquad (2)$$

where $\lambda$ is the X-ray wavelength. Estimated sizes are ~10.7 nm, ~11.1 nm, and ~11.9 nm for the nanoparticles and hybrids with the $rGO/ZnFe_2O_4$ of 0.05 and 0.10, respectively. The strongest (311) peak shifts from ~35.18° to higher ~35.38° and ~35.42° as increasing $rGO/ZnFe_2O_4$ ratio form 0 to 0.05 and 0.10 (Fig. 1b). This indicates a lattice shrink on basis of Bragg's equation. The increase in the average particle size and lattice shrink could imply that the rGO favors the growth and crystallization of the $ZnFe_2O_4$ crystallites.

## 3.2 SEM Analysis

Fig. 2 shows typical SEM micrographs of the nanoparticles and hybrids. The $ZnFe_2O_4$ nanoparticles show granular particle morphology. As the graphene is introduced, the nanoparticles show similar particle morphology. But the partial nanoparticles are completely adhered on the reduced graphene oxide, forming large platelike morphology. The nanoparticles in three samples have average particle size of ~16 nm, closed to the result determined by XRD analysis.

## 3.3 Raman and FTIR Spectra Analyses

Raman spectroscopy, a nondestructive method, is also a useful technique to explore the crystalline or molecular changes after hydrogenation via molecular vibrations. Fig. 3a

3

shows the Raman spectrum of the nanoparticles and hybrids. The Stokes phonon energy of graphene shifts and the laser excitation creates two main band structures. The band centered at ~1348 cm$^{-1}$ is a primary in-plane vibrational mode (D-band) in the hexagonal graphitic layers. The second-order overtone of a different in-plane vibration of sp$^2$ hybridization of the carbon atom in the graphene sheet is observed at ~1603 cm$^{-1}$

called the G-band. The D-band corresponds to the edge disordered band structure of k-point phonon of A$_{1g}$ symmetry carbon atoms and the G-band corresponds to the E$_{2g}$ mode of order band structure of sp$^2$ hybridization of carbon atoms. The disorder nature of graphene increases as the Raman intensity increases. The defects are related to the I$_D$/I$_G$ ratio, the intensity of the peaks. The value of I$_D$/I$_G$ for the hybrids
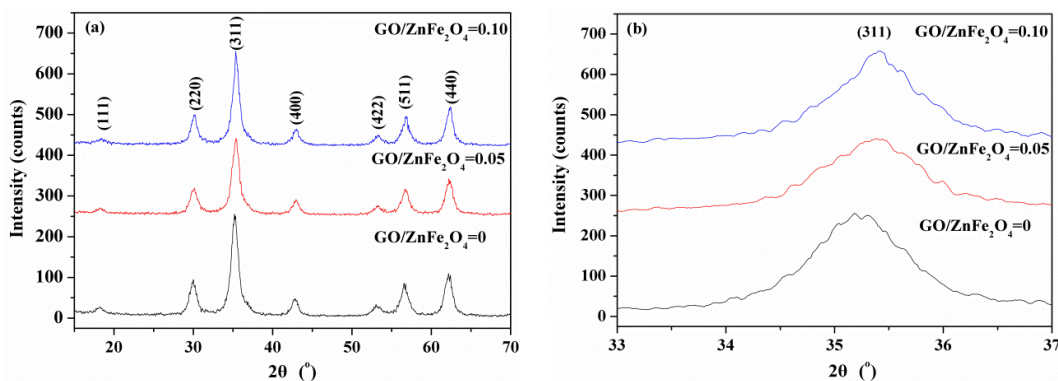


**Fig. 1. (a) XRD patterns and (b) strongest (311) XRD peak patterns of the ZnFe$_2$O$_4$ particles and hybrids**
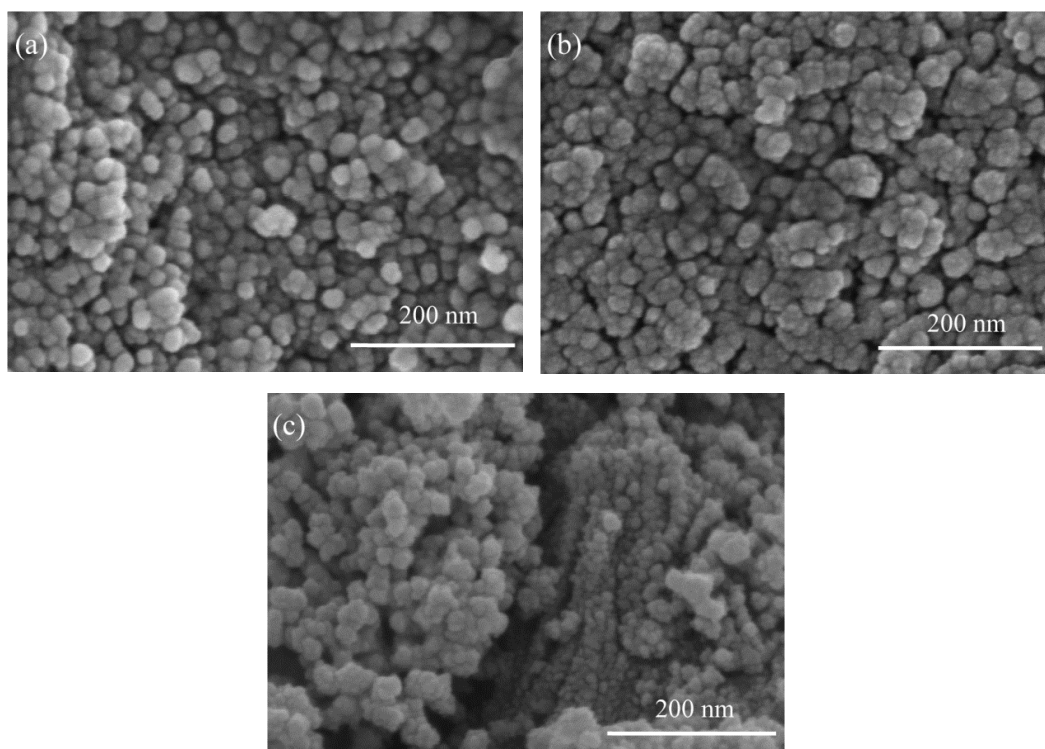


**Fig. 2. SEM micrographs of (a) the ZnFe$_2$O$_4$ particles and the hybrids with rGO/ZnFe$_2$O$_4$ mass ratio of (b) 0.025, and (c) 0.050**

with rGO/ZnFe$_2$O$_4$ of 0.05 and 0.10 is 1.15 and 1.16, respectively, which is higher than that of GO (0.86). The increased I$_D$/I$_G$ is attributed to the formation of new and smaller sp$^2$ domains during the reduction, giving evidence that the GO was successfully reduced to graphene. The GO could be mainly reduced in the hydrothermal process. The peaks centered at ~317, ~470, ~593 and ~616 cm$^{-1}$ are related to the distinct vibrational modes of the hexagonal ZnFe$_2$O$_4$ nanoparticles.

The synthesized ZnFe$_2$O$_4$ nanoparticles and hybrids were further investigated by FT-IR measurement. As shown in Fig. 3b, the strong and overlapping band centered at ~3421 cm$^{-1}$ is assigned to the stretching vibration of structural O−H and H–O–H in adsorbed water molecules. The peaks at ~1591 cm$^{-1}$ are assigned to H–O–H bending vibration in water molecular or OH deformation vibration due to surface hydroxyls. The intensity of these two peaks of the hybrids are more intense than that of the nanoparticles. This implies that the hybrids are more hydrophylic and so will have higher photocatalytic activity. The absorption peak centered at ~573 cm$^{-1}$ is assigned as the vibration of ferrite groups [16], corresponding to the tetrahedral sites of positive ions in the ferrite [16]. This peak shifts to low wavenumber as the increase in rGO/ZnFe2O4 ratio, indicating the decrease in distance between Fe$^{3+}$–O$^{2-}$ in the tetrahedral sites. This confirms the formation of ZnFe$_2$O$_4$ structure. Moreover, the stretching vibrations of C−OH, C−O−C and C−O, which is centered at 1380, 1270, and 1050 cm$^{-1}$ [17], are not observed in the spectra. This further indicates that GO has been reduced to rGO in our reaction system. The results agree well with the result of XRD and further confirm that the ZnFe$_2$O$_4$ nanoparticles and ZnFe$_2$O$_4$/rGO hybrids can be obtained by our simple method.
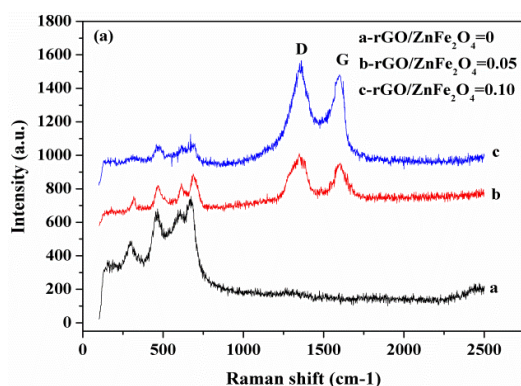
## 3.4 Optical Absorption Analysis

Figs. 4a and 4b shows the transmittance (*T*) and reflectance (*R*) spectra of the nanoparticles and hybrids.in the wavelength range of 330–850 nm. The optical bandgap can be determined with absorption edge (*λ*$_e$) from absorbance spectra (Fig, 4c) by the relation *E*$_g$=1240/*λ*$_e$, which gives the smaller *E*$_g$ in the range of ~1.70−1.78 eV. The optical band gap (*E*$_g$) can also be calculated with the following Tauc's relationship [18]:

$$(\alpha h v)^n = C(h v - E_g) \tag{3}$$

Where *h*v is photon energy and C is a constant, and *α* is absorption coefficient and can be calculated by equation [19]:

$$\alpha = \frac{1}{d} \ln \frac{1-R}{T} \tag{4}$$

where *d* is the thin layer thickness. For the allowed direct bandgap, the *n* equals 2. Fig. 4d shows the plots of (*αhv*)$^2$ vs. photon energy *hv*. The straight-line portion of the curve, when extrapolated to zero, gives the optical direct bandgap *E*$_g$ in the range of ~2.0−2.1 eV. These *E*$_g$ should be weighted average values of the ZnFe$_2$O$_4$ nanoparticles and rGO, and so are narrowed as increasing rGO content.

## 3.5 Photocatalysis of the Nanoparticles and Hybrids

Fig. 5 shows the concentration variations of the malachite green aqueous solutions in the various conditions on the nanoparticles and hybrids in the sunlight. The graphs of ln(*C*$_0$/*C*) versus reactiontime *t* are show in Fig. 6.
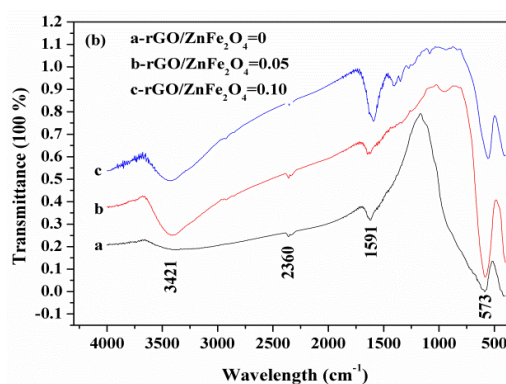


Fig. 3. (a) Raman spectra and (b) FT-IR spectra of the ZnFe$_2$O$_4$ particles and Hybrids

These graphs are more abrupt in first 30 min than following process, which could be related to the adsorption of the dye on the nanoparticles and hybrid. The plots are approximately linear in 60−180 min. Using the slopes of the plots in 60−180 min, the quasi-kinetic apparent rate constants ($k_1$) are obtained to be in the range of ~0.41–0.96 h$^{-1}$ (Table 1). The $k_1$ of the hybrids show larger than that of the nanoparticles and increased as the increase of rGO/ZnFe$_2$O$_4$ ratio. The $k_1$ is also larger at initial pH=5 than at pH=7. Moreover, the H$_2$O$_2$ remarkably speeds up the dye photodegradation, almost completely decomposing the dye in 30 min (Fig. 7). This indicates a photo-Fenton-like reaction. The plots of ln($C_0$/$C$) versus reaction time $t$ are showed in Fig. 8. These plots are more abrupt in initial period of 5 min, which could also be mainly related to the adsorption of the dye on the nanoparticles and hybrid. With the approximate slopes of the plots in 5-30 min, the quasi-kinetic apparent rate constants ($k_1$) are estimated to be in the range of ~3.86–7.53 h$^{-1}$ (Table 1). The $k_1$ of the hybrids are larger than that of the nanoaprticles and increased as the increase of rGO/ZnFe$_2$O$_4$ ratio and H$_2$O$_2$ concentration. The percentage removal efficiency of the dye solution is listed in Table 2.
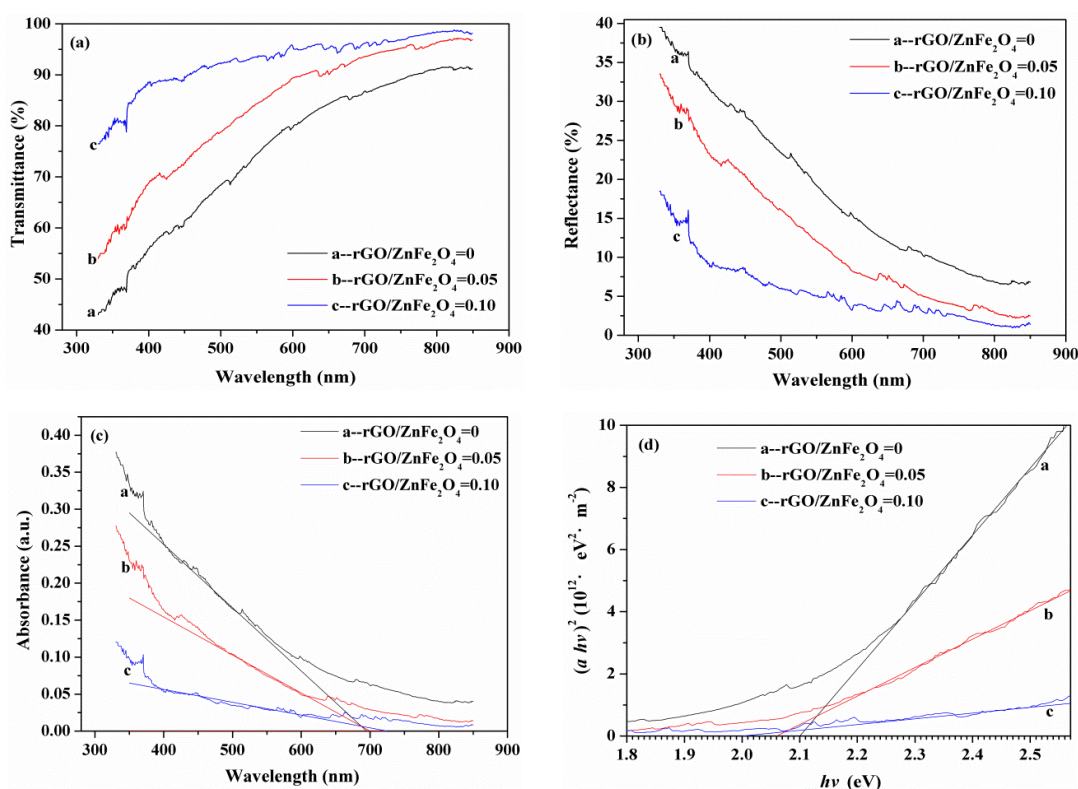


**Fig. 4. (a) Transmittance, (b) reflectance spectra, and (c) absorbance spectra and (d) plots of ($\alpha h\nu$)$^2$ versus $h\nu$ and of the ZnFe$_2$O$_4$ particles and hybrids**

**Table 1. The quasi-kinetic constants $k_1$ (h$^{-1}$) under irradiation of the sunlight in various initial pH and H$_2$O$_2$ aqueous solution amounts**

| rGO/ZnFe$_2$O$_4$ | pH=5 H$_2$O$_2$: 0 ml | pH=7 H$_2$O$_2$: 0 ml | pH=7 H$_2$O$_2$: 0.5 ml | pH=7 H$_2$O$_2$: 1.0 ml |
|---|---|---|---|---|
| Blank | 0.25 | 0.23 | 1.51 | 1.60 |
| 0 | 0.43 | 0.41 | 3.86 | 4.68 |
| 0.05 | 0.72 | 0.68 | 4.67 | 6.51 |
| 0.10 | 0.96 | 0.73 | 6.50 | 7.53 |

**Table 2. The percentage removal efficiency of the dye solution in various initial pH and $H_2O_2$ aqueous solution amounts under irradiation of the sunlight**

| rGO/ZnFe$_2$O$_4$ | pH=5 | pH=7 | pH=7 | pH=7 |
| --- | --- | --- | --- | --- |
| | H$_2$O$_2$: 0 ml | H$_2$O$_2$: 0 ml | H$_2$O$_2$: 0.5 ml | H$_2$O$_2$: 1.0 ml |
| Blank | 52.2 | 49.9 | 53.1 | 55.2 |
| 0 | 80.1 | 76.9 | 91.9 | 95.1 |
| 0.05 | 92.7 | 90.3 | 95.2 | 98.3 |
| 0.10 | 96.3 | 93.8 | 97.8 | 98.9 |
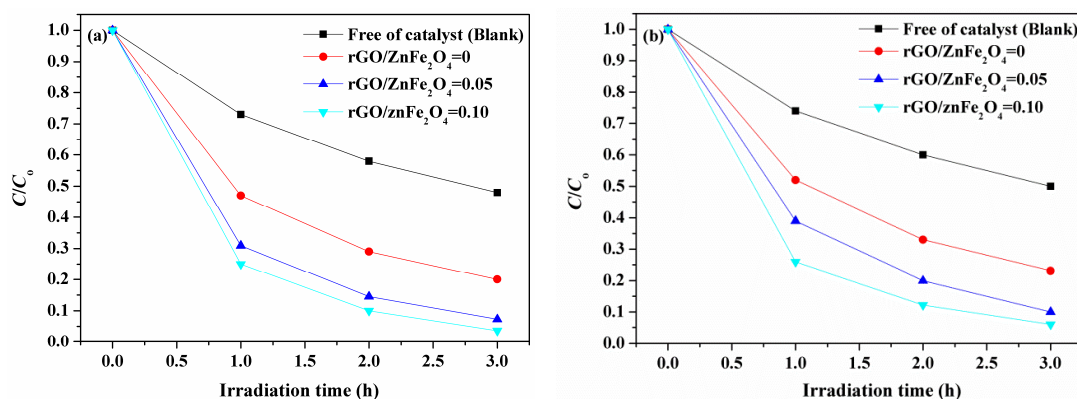


**Fig. 5. Variations of the malachite green concentrations in the water with initial pH= (a) 5 and (b) 7 with the irradiation time of the sunlight**
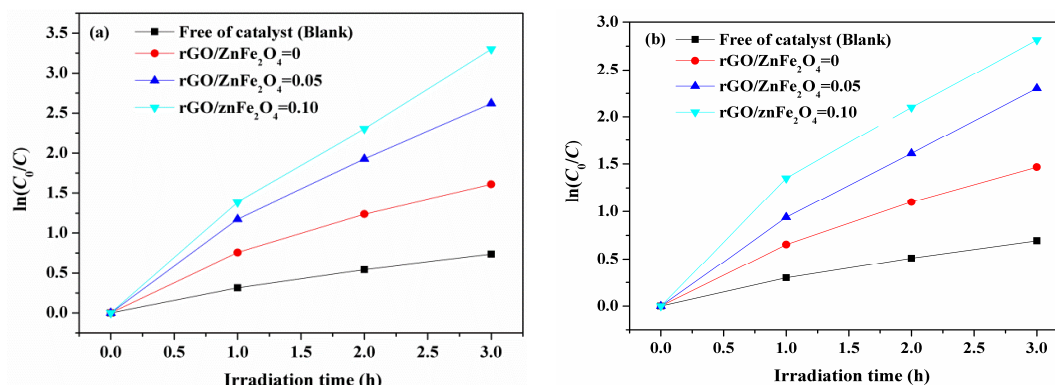


**Fig. 6. Plots of ln($C_0$/$C$) vs. irradiation time (t) for the photodegradation of the malachite green in the water with initial pH=(a) 5 and (b) 7 with the irradiation time of the sunlight**

With the calculation methods applied by Butler et al. [20] and Pineda et al. [21], the absolute work function ($\chi$) of intrinsic ZnFe$_2$O$_4$ and rGO can be calculated to be 5.91 eV and 6.43 eV, respectively. The energy levels of absolute conduction and valence bands ($E_c$ and $E_v$) of ZnFe$_2$O$_4$ can be calculated by the following relation [20]:

$$E_c = \chi + \frac{E_g}{2} \qquad (5)$$

$$E_v = \chi - \frac{E_g}{2} \qquad (6)$$

In term of average band gap of ~1.94 eV of pure ZnFe$_2$O$_4$, as estimated from the optical spectra, the $E_c$ and $E_v$ of the ZnFe$_2$O$_4$ equals to 6.88 eV and 4.94 eV. The schematic diagram of energy levels and initial redox process of the rGO/ZnFe$_2$O$_4$ heterostructure under sunlight excitation can be proposed in Fig. 9. The conduction band energy level of the ZnFe$_2$O$_4$ is higher than that of rGO, leading to that the electrons in the ZnFe$_2$O$_4$ can be transferred to the rGO. In the diagram, the increased number of electrons in the rGO can be used as reducing agents to directly reduce the dye or produce OH, or result in the formation of reactive oxygen-

based radicals, such as $O^{2-}$. The $O^{2-}$ upon protonation produces hydroperoxy radicals ($HO_{-}^{2\cdot}$) and eventually hydroxyl radicals ($OH_{-}$) are formed [22,23]. The remaining electrons in the $ZnFe_2O_4$ conduction band (CB) can also either directly reduce the dye or react with adsorbed water molecules and surface $OH_{-}$ groups, producing $OH_{-}$ [23,24]. The holes in the $ZnFe_2O_4$ valence band (VB) can be used as oxidizing agents directly oxidize the dye,

or react with adsorbed water molecules and surface $OH_{-}$ groups, producing $\cdot OH$ [23,24]. Thus, the recombination of photo-generated electrons and holes can be prevent, and so the photocatalytic activity of the nanoparticles and hybrids can be enhanced. With the increase of photo-generated electrons and holes as increasing $rGO/ZnFe_2O_4$ ratio, the photocatalytic activity of the hybrids can be further enhanced.
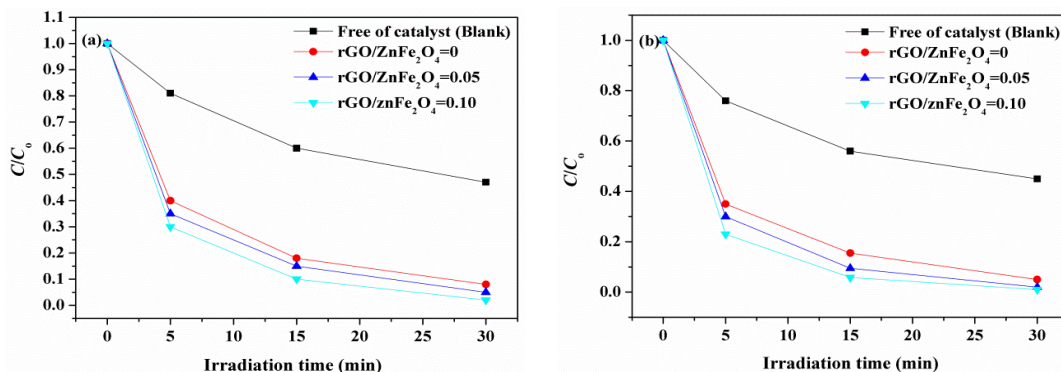


**Fig. 7. Variations of the malachite green concentrations in the water with initial pH=7 and different $H_2O_2$ aqueous solution amounts of (a) 0.5 ml and (b) 1.0 ml as function of the irradiation time of the sunlight**
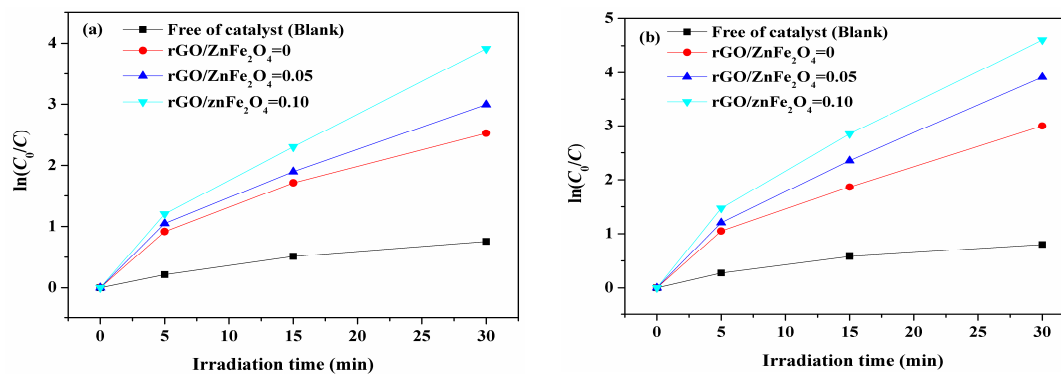


**Fig. 8. Plots of $\ln(C_0/C)$ vs. irradiation time (t) for the photodegradation of the malachite green in the water with initial pH=7 and different $H_2O_2$ aqueous solution amounts of (a) 0.5 ml and (b) 1.0 ml**
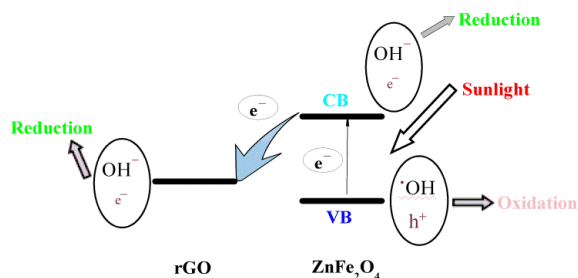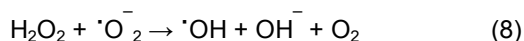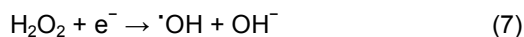


**Fig. 9. Schematic diagram of energy levels and initial redox process of the hybrids in the process of sunlight excitation**

8

The $H_2O_2$ is considered to have two functions in the photocatalytic process [25]. It accepts a photogenerated electron to form $\cdot OH$ radical (Reaction (7)). In addition, it forms $\cdot OH$ radicals according to Reaction (8)

$$H_2O_2 + e^- \rightarrow \cdot OH + OH^- \tag{7}$$

$$H_2O_2 + \cdot O_2^- \rightarrow \cdot OH + OH^- + O_2 \tag{8}$$

The $\cdot OH$ and $OH^-$ radicals play oxidation and reduction roles in the photodegradation process, respectively. The concentration increases of photo-generated electrons/holes and $\cdot OH/OH^-$ as the increase of $rGO/ZnFe_2O_4$ ratio and $H_2O_2$ concentration leads to the enhanced Fenton-like reaction in the dye photodegradation.

The oxidation-reduction characteristics of the photocatalyst surface and its evident variation have considerable influence on the activities of the catalysts and photocatalysts [26−29]. The oxidation-reduction characteristics of the photocatalyst surface is associated with its intrinsic behavior and environment, and usually evaluated by oxidation-reduction potential (ORP) [24−26]. The ORP of the nanoparticles and hybrids surfaces are showed in Fig. 10. The ORP of the hybrids is overall smaller than that of the nanoparticles and decreases as increasing $rGO/ZnFe_2O_4$ ratio. This could implies that more photogenerated electrons take effect and/or the photogenerated electrons play dominant role in the process of the dye photodegradation due to rGO introduction. Moreover, the ORP is larger at initial pH=5 than pH=7 in the absence of $H_2O_2$, which could be ascribed to the more reducing characteristics of the photogenerated electron at high pH [28]. Furthermore, the $H_2O_2$ leads to the slowdown decrease of the ORP with the $rGO/ZnFe_2O_4$. Although the ORP is higher at low $H_2O_2$ concentration.
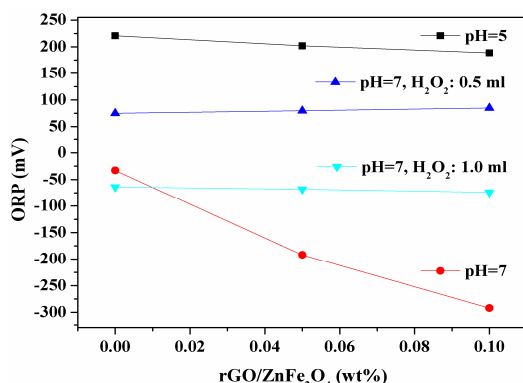
## 3.6 Magnetic and Magnetic Separation Properties of the Nanoparticles and Hybrids

Fig. 11 shows the room temperature hysteresis loops of the $ZnFe_2O_4$ and hybrids. The samples are all ferromagnetic. With increasing applied field, the magnetization of the $ZnFe_2O_4$ nanoparticles increases, and nearly reaches saturation state under highest magnetic fields of 30 KOe. Maximum magnetization of the nanoparticles at applied field of 30 KOe (identified as a saturation magnetization $M_s$) is in the range of ~25.15−26.28 emu/g. The Ms slightly decreases with the increase of rGO content, which is ascribed to the increase of rGO content. The coercivity ($H_c$) of the nonaparticles and hybrids is ~28.1 Oe. Large saturation magnetization makes the nanoparticle and hybrids show good magnetic separation performance from the degraded solutions (Fig. 12).
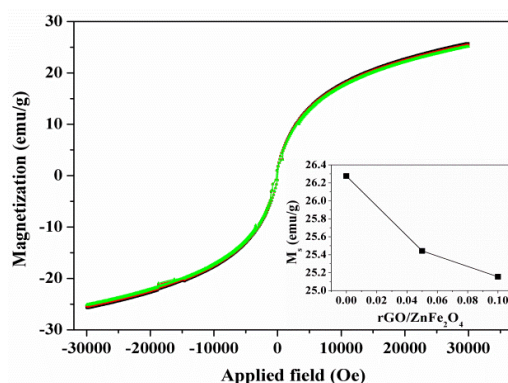


**Fig. 11. Room temperature hysteresis loop of the $ZnFe_2O_4$ particles and hybrids**





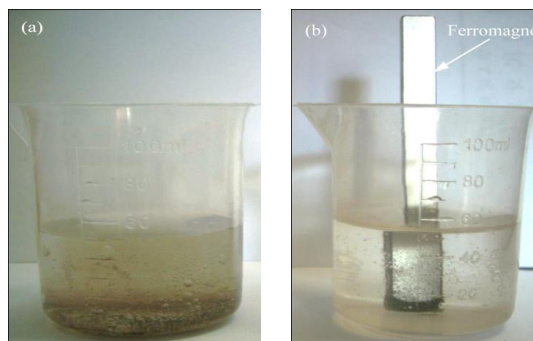**Fig. 10. ORP of the $ZnFe_2O_4$ particles and hybrids in the photocatalysis systems**

**Fig. 12. The image of magnetic separation of the $ZnFe_2O_4$ particles and hybrids from the degraded aqueous solution**
*(a) before (b) after magnet attraction*

9

## 4. CONCLUSIONS

The $ZnFe_2O_4$ nanoparticles and $ZnFe_2O_4$-rGO hybrids with rGO/$ZnFe_2O_4$ mass ratio of 0.05 and 0.10 were synthesized by a hydrothermal method. The effects of the rGO/$ZnFe_2O_4$ mass ratio on the photocatalytic activity were studied for the first time. Room temperature XRD, Raman and FTIR analyses confirmed the formation of crystalline $ZnFe_2O_4$. Raman and FTIR analyses also revealed that the graphene oxide was reduced. The SEM analysis showed that nanoparticles had a uniform granular morphology and nanoscale size of ~16 nm. Under sunlight excitation, the high photocatalytic and Fenton-like photocatalytic activities of the nanoparticles and hybrids was observed in the photodegradation of malachite green in the water. The degradation rates on the hybrids are higher than that on the nanoparticles and increased with the increase of rGO/$ZnFe_2O_4$ ratio and decrease of initial pH. Whereas, the photo-Fenton-like reaction is intenser at higher $H_2O_2$ concentration. The quasi-kinetic rate constants were in the range of ~0.414–0.96 $h^{-1}$ and remarkably increased to ~3.86–7.53 $h^{-1}$ as using $H_2O_2$. The synthesized nanoparticles and hybrids showed large saturation magnetization of ~25.15−26.28 emu/g, which provided a well magnetic separation performance from the photodegraded solution.

## COMPETING INTERESTS

Authors have declared that no competing interests exist.

## REFERENCES

1. Kavitha T, Gopalan AI, Lee K-P, Park S-Y. Glucose sensing, photocatalytic and antibacterial properties of graphene–ZnO nanoparticle hybrids. Carbon. 2012;50: 2994–3000.
2. Zhang N, Zhang Y, Xu YJ. Recent progress on graphene-based photocatalysts: Current status and future perspectives. Nanoscale. 2012;4:5792–5813.
3. Zhang N, Zhang Y, Yang MQ, Tang ZR, Xu YJ. A critical and benchmark comparison on graphene-, carbon nanotube-, and fullerene-semiconductor nanocomposites as visible light photocatalysts for selective oxidation. J. Catal. 2013;299:210–221.
4. Enmin Zong, Dan Wei, Haiqin Wan, Shourong Zheng, Zhaoyi Xu, Dongqiang Zhu. Adsorptive removal of phosphate ions from aqueous solution using zirconia-functionalized graphite oxide. Chem. Eng. J. 2013;211:193–20394
5. Jun Zhang, Jiaguo Yu, Mietek Jaroniec, Jian Ru Gong. Noble metal-free reduced graphene oxide-$Zn_xCd_{1−x}S$ nanocomposite with enhanced solar photo-catalytic $H_2$-production performance. Nano Lett. 2012; 12(9):4584–4589
6. Zhang Y-H, Zhang N, Tang ZR, Fu X, Xu Y-J. Graphene transforms wide band gap ZnS to a visible light photocatalyst. The new role of graphene as a macromolecular photosensitizer. ACS Nano. 2012;6:9777–9789.
7. Zhang N, Zhang Y, Pan X, Yang MQ, Xu YJ. Constructing ternary CdS–graphene–$TiO_2$ hybrids on the flatland of graphene oxide with enhanced visible-light photoactivity for selective transformation. J. Phys. Chem. C. 2012;116:18023–18031.
8. Fu D-Y, Han G-Y, Chang Y-Z, Dong J-H. The synthesis and properties of ZnO–graphene nano hybrid for photo-degradation of organic pollutant in water. Mater. Chem. Phys. 2012;132:673–681.
9. Chen Z, Zhang N, Xu YJ. Synthesis of graphene–ZnO nanorod nanocomposites with improved photoactivity and anti-photocorrosion. Cryst. Eng. Commun. 2013;15:3022–3030.
10. Shuying Dong, Yukun Li, Jingyu Sun, Chongfei Yu, Yihui Li, Jianhui Sun. Facile synthesis of novel ZnO/RGO hybrid nanocomposites with enhanced catalytic performance for visible-light-driven photodegradation of metronidazole. Mater. Chem. Phys. 2014;145:357–365.
11. Li Liu, Chao Dong, Kong-Lin Wu, Yin Ye, Xian-Wen Wei. Synthesis of nitrogen-doped graphene–ZnO nanocomposites with improved photocatalytic activity. Mater. Lett. 2014;129:170–173.
12. Thangavel S, Elayaperumal M, Venugopal G. Synthesis and properties of tungsten oxide and reduced graphene oxide nanocomposites. Mater. Express. 2012;2: 327–334.
13. Peng Gao, Jincheng Liu Darren Delai Sun, Wunjern Ng. Graphene oxide–CdS composite with high photocatalytic degradation and disinfection activities under visible light irradiation. J. Hazard. Mater. 2013;250-251:412-420.
14. Zhang N, Zhang Y, Pan X, Fu X, Liu S, Xu YJ. Assembly of CdS nano-particles on the two-dimensional graphene scaffold as

visible-light-driven photo-catalyst for selective organic transformation under ambient conditions. J. Phys. Chem. C. 2011;115:23501–23511.

15. Nan Zhang, Min-Quan Yang, Zi-Rong Tang, Yi-Jun Xu. CdS–graphene nano-composites as visible light photocatalyst for redox reactions in water: A green route for selective transformation and environmental remediation. Journal of Catalysis. 2013;303:60–69.

16. Ashok B Nawale, Nilesh S Kanhe, Patil KR, Bhoraskar SV, Mathe VL, Das AK. Magnetic properties of thermal plasma synthesized nanocrystalline nickel ferrite ($NiFe_2O_4$). J. Alloys Compd. 2011;509: 4404–4413.

17. Feng C-L, Zhang L, Yang M-H, Song X-Y, Zhao H, Jia Z, Sun K-N, Liu G. One-pot synthesis of copper sulfide nanowires/reduced graphene oxide nanocomposites with excellent lithium-storage properties as anode materials for lithium-ion batteries. ACS Appl. Mater. Interfaces. 2015;7:15726−15734.

18. Chen JL, Chen D, He JJ, Zhang SY, Chen ZH. The microstructure, optical, and electrical properties of sol–gel-derived Sc-doped and Al–Sc co-doped ZnO thin films. Appl. Surf. Sci. 2009;255:9413–9419.

19. Pathan HM, Desai JD, Lokhande CD. Modified chemical deposition and physico-chemical properties of copper sulphide (Cu2S) thin films. Appl. Surf. Sci. 2002;202:47.

20. Butler MA, Ginley DS. Prediction of flatband potentials at semiconductor-electrolyte interfaces from atomic electronegativities. J. Electrochem. Soc. 1978;125(2):228-232.

21. Hölzl J, Schulte FK. Work function of metals, in Solids surface Science G. Höhler, editor, Springer-Verlag, Berlin; 1979.

22. Ollis D, Pichat P, Serpone N. $TiO_2$ photocatalysis-25 years. Appl. Catal. B. 2010;99:377.

23. Christoforidis KC, Sengele A, Keller V, Keller N. Single-step synthesis of $SnS_2$ nanosheet-decorated $TiO_2$ anatase nanofibers as efficient photocatalysts for the degradation of gas phase diethylsulfide. ACS Appl. Mater. Interfaces. 2015;7(34): 19324–19334

24. Zhang Z, Shao C, Li X, Sun Y, Zhang M, Mu J, Zhang P, Guo Z, Liu Y. Hierarchical assembly of ultrathin hexagonal $SnS_2$ nanosheets onto electrospun $TiO_2$ nanofibers: Enhanced photocatalytic activity based on photoinduced interfacial charge transfer. Nanoscale. 2013;5: 606−618.

25. Emad S Elmolla, Malay Chaudhuri. Photocatalytic degradation of amoxicillin, ampicillin and cloxacillin antibiotics in aqueous solution using UV/$TiO_2$ and UV/$H_2O_2$/$TiO_2$ photocatalysis. Desalination. 2010;252(1–3):46–52.

26. Agustina TE, Ang HM, Vareek VK. A review of synergistic effect of photo-catalysis and ozonation on wastewater treatment. J. Photochem. Photobiol. C: Photochem. Rev. 2005;6:264–273.

27. Bahnemann DW, Cunningham J, Fox MA, Pelizzetti E, Pichat P, Serpone N. In Zepp RG, Heltz GR, Crosby DG (Eds.) Aquatic Surface Photochemistry. Lewis Publishers, Boca Raton. 1994;261.

28. White JR, Bard AJ. Electrochemical investigation of photocatalysis at cadmium sulfide suspensions in the presence of methyl viologen. J. Phys. Chem. 1985;89: 1947–1954.

29. Kaur S, Singh V. $TiO_2$ mediated photocatalytic degradation studies of Reactive Red 198 by UV irradiation. J. Hazard. Mater. 2007;141:230–236.